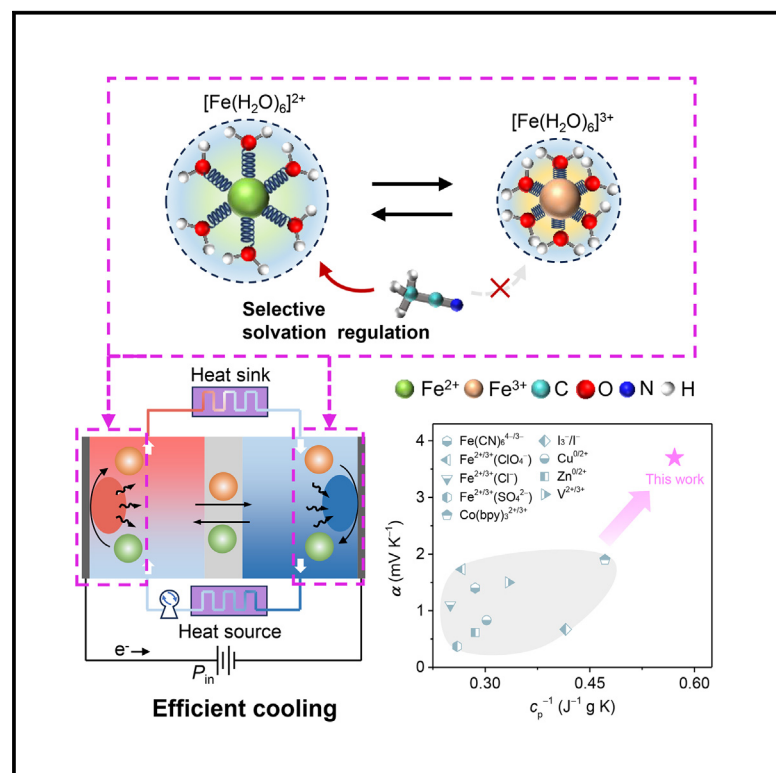


# Solvation entropy engineering of thermogalvanic electrolytes for efficient electrochemical refrigeration

## Graphical abstract



## Authors

Yilin Zeng, Boyang Yu, Ming Chen, ..., Guang Feng, Jun Zhou, Jiangjiang Duan

## Correspondence

gfeng@hust.edu.cn (G.F.),  
jiangjduan@hust.edu.cn (J.D.)

## In brief

Emerging thermogalvanic systems can not only convert heat into electricity but also enable electrochemical refrigeration. However, their cooling performance is impeded by developing high-temperature coefficient electrolytes with low heat capacity. Herein, we report a synergistic solvent and anion engineering strategy to tackle the above challenge. The optimized electrolyte achieves over a 70% improvement in cooling power and a temperature drop of  $\sim 1.42 \text{ K}$  with only  $0.11 \text{ W cm}^{-2}$  input. This work provides an effective guiding principle for designing thermogalvanic electrolytes.

## Highlights

- Synergistic solvent and anion engineering enables efficient thermogalvanic cooling
- Iron-based electrolyte achieves a high-temperature coefficient of  $3.73 \text{ mV K}^{-1}$
- Over 70% improvement in cooling power was measured with a potential COP of 14.3
- A direct cooling of electrolyte  $\sim 1.42 \text{ K}$  was demonstrated with only  $0.11 \text{ W cm}^{-2}$  input

Zeng et al., 2025, Joule 9, 101822

March 19, 2025 © 2025 Elsevier Inc. All rights are reserved, including those for text and data mining, AI training, and similar technologies.

<https://doi.org/10.1016/j.joule.2025.101822>



## Article

# Solvation entropy engineering of thermogalvanic electrolytes for efficient electrochemical refrigeration

Yilin Zeng,<sup>1,5</sup> Boyang Yu,<sup>2,5</sup> Ming Chen,<sup>3,5</sup> Jinkai Zhang,<sup>3</sup> Pei Liu,<sup>1</sup> Jinhua Guo,<sup>1</sup> Jun Wang,<sup>4</sup> Guang Feng,<sup>3,\*</sup> Jun Zhou,<sup>1</sup> and Jiangjiang Duan<sup>1,6,\*</sup>

<sup>1</sup>Wuhan National Laboratory for Optoelectronics, School of Optical and Electronic Information, Huazhong University of Science and Technology, Wuhan 430074, China

<sup>2</sup>Beijing Institute of Nanoenergy and Nanosystems, Chinese Academy of Sciences, Beijing 101400, China

<sup>3</sup>State Key Laboratory of Coal Combustion, School of Energy and Power Engineering, Huazhong University of Science and Technology, Wuhan 430074, China

<sup>4</sup>School of Physics and Optoelectronic Engineering, Shandong University of Technology, Zibo 255000, China

<sup>5</sup>These authors contributed equally

<sup>6</sup>Lead contact

\*Correspondence: [gffeng@hust.edu.cn](mailto:gffeng@hust.edu.cn) (G.F.), [jiangjduan@hust.edu.cn](mailto:jiangjduan@hust.edu.cn) (J.D.)

<https://doi.org/10.1016/j.joule.2025.101822>

**CONTEXT & SCALE** With global warming and industrial and artificial intelligence blooming, the substantial heat emission emphasizes the need for efficient and eco-friendly cooling technologies. Emerging electrochemical refrigerator is one of the promising candidates due to the inexpensive, flexible, and scalable merits. Nevertheless, their cooling performance is urgent to improve by developing thermogalvanic electrolytes with high-temperature coefficients and low heat capacity. Herein, we report a synergistic binary solvent and anion engineering strategy, which enables weak  $\text{Fe}^{2+/3+}$ - $\text{ClO}_4^-$  interactions and selective solvation arrangement of  $\text{Fe}^{2+}$  by nitrile solvents. As a result, the temperature coefficient was boosted to as high as  $3.73 \text{ mV K}^{-1}$  with a decreased heat capacity. This electrolyte could potentially support a coefficient of performance of 14.3 with  $\sim 70\%$  enhanced cooling power. Furthermore, a direct cooling of electrolyte  $\sim 1.42 \text{ K}$  was demonstrated with only  $0.11 \text{ W cm}^{-2}$  input.

## SUMMARY

Emerging thermogalvanic systems can not only convert heat into electricity but also enable electrochemical refrigeration. However, their fundamental electrolytes meet challenges toward high cooling performance due to the absence of rational design principles. Developing thermogalvanic electrolytes with high-temperature coefficients and low heat capacity is the key to efficient electrochemical refrigeration. Here, we report an iron-based electrolyte design strategy by synergistic binary solvent and anion engineering, which rearranges the solvation shell of  $\text{Fe}^{2+/3+}$  ions to achieve a high-temperature coefficient of  $3.73 \text{ mV K}^{-1}$  with decreased heat capacity. The comprehensive analyses reveal that the weak  $\text{Fe}^{2+/3+}$ - $\text{ClO}_4^-$  interactions, accompanied by selective association between  $\text{Fe}^{2+}$  and nitrile solvents, fully enlarge the entropy change available for electrochemical refrigeration. As a result, the optimized electrolyte could potentially reach  $\sim 70\%$  improvement of cooling power, and a direct cooling of electrolyte  $\sim 1.42 \text{ K}$  was demonstrated with only  $0.11 \text{ W cm}^{-2}$  input, showing promise for practical electrochemical refrigeration.

## INTRODUCTION

The fast growth of global cooling demand, accompanied by significant energy consumption and greenhouse emissions, has spurred the seeking of efficient and eco-friendly cooling technologies.<sup>1–3</sup> Currently, the majority of cooling demand is met by vapor compression refrigeration, which poses substantial envi-

ronmental concerns due to the refrigerants.<sup>4,5</sup> Emerging alternatives, represented by Peltier semiconductors,<sup>6,7</sup> caloric materials,<sup>8,9</sup> and thermogalvanic systems,<sup>10,11</sup> offer a promising way to zero-global-warming-potential solutions. Among these, thermogalvanic systems stand out by facilitating a direct and continuous cooling of electrolytes (namely refrigerant) through an endothermic redox reaction, while heat is pumped via



the reverse exothermic process. The entropy change ( $\Delta S$ ) for such electrochemical refrigeration typically stands at  $\sim 100 \text{ J mol}^{-1} \text{ K}^{-1}$ , underscoring its substantial theoretical cooling potential compared with other technologies.<sup>12</sup> Furthermore, unlike the solid-state thermoelectric refrigeration system, the electrochemical refrigeration leveraging liquid electrolytes offers advantages such as flexibility, scalability, and low cost. These systems can be evolved into the flow devices and wearable devices for potential applications such as thermal management of lithium battery packs, human body cooling, and industrial-grade cooling.<sup>13–17</sup> Regrettably, the experimental cooling capability of thermogalvanic systems is generally limited to 0.1 K.<sup>10–12</sup> To date, most studies have focused on system design and numerical simulation for electrochemical refrigeration,<sup>18–20</sup> while the critical challenge of designing effective electrolytes remains unresolved, severely impeding practical applications.

In general, the efficiency of cooling technologies is typically assessed using a dimensionless parameter known as the coefficient of performance (COP), defined as the ratio of useful cooling energy generated to the work input ( $\text{COP} = Q_c/W_{in}$ ).<sup>3</sup> For thermogalvanic systems (see Note S1 for details), the  $Q_c$  is proportional to the temperature coefficient ( $\alpha$ ), which dominates the magnitude of COP. The  $\alpha$  of thermogalvanic electrolyte depicts the entropy change ( $\Delta S$ ) during the redox reaction between redox species, given by  $\alpha = \Delta S/nF$ , where  $n$  is the number of electrons transferred and  $F$  is the Faradaic constant.<sup>10,20</sup> An ideal thermogalvanic electrolyte for electrochemical refrigeration is expected to possess a high  $\alpha$  to generate considerable  $Q_c$  and a low specific heat capacity ( $c_p$ ) to achieve an apparent temperature drop.

Iron-based thermogalvanic electrolytes, such as  $\text{Fe}^{2+/3+}$  and  $[\text{Fe}(\text{CN})_6]^{3-/4-}$ , are popular due to their intrinsic large solvation structural entropy difference and cost-effectiveness.<sup>21–23</sup> Particularly, great advances in  $[\text{Fe}(\text{CN})_6]^{3-/4-}$  electrolytes have been achieved for efficient heat harvesting.<sup>24–32</sup> The unique packed solvation structure of  $[\text{Fe}(\text{H}_2\text{O})_6]^{2+/3+}$  endows an ideal  $\Delta S$  of approximately  $174 \text{ J mol}^{-1} \text{ K}^{-1}$ , surpassing the benchmark of  $\sim 135 \text{ J mol}^{-1} \text{ K}^{-1}$  for  $[\text{Fe}(\text{CN})_6]^{3-/4-}$ , making it a promising candidate for electrochemical refrigeration.<sup>33–36</sup> However, the strong coordination of  $\text{Fe}^{2+/3+}$  with anions would remarkably reduce the actual  $\Delta S$ , leading to a limited  $\alpha$  ( $\sim 0.2$ – $1.5 \text{ mV K}^{-1}$ ).<sup>36–38</sup> In attempts to enhance  $\alpha$ , some studies have explored the utilization of  $\text{Fe}^{2+/3+}$  in organic solvents.<sup>39–41</sup> Unfortunately, the strong interaction between  $\text{Fe}^{2+/3+}$  and anions has limited the accessible concentration of less than 10 mM, meaning poor ionic conductivity and cooling power. Besides, another serious problem is the high specific heat capacity of water ( $c_p \sim 4.2 \text{ J g}^{-1} \text{ K}^{-1}$ ) that causes current aqueous electrolytes to nearly fail to exhibit a temperature drop in practical operation. Therefore, rational design of thermogalvanic electrolytes is urgent to tackle these challenges and advance the efficiency of electrochemical refrigeration systems.

Here, we proposed a synergistic strategy to mitigate the  $\text{Fe}^{2+/3+}$ -anion interactions and enlarge the entropy change ( $\Delta S$ ) for  $\text{Fe}^{2+/3+}$ , by employing  $\text{ClO}_4^-$  as a counterion and developing a binary solvent of nitriles and water. The presence of  $\text{ClO}_4^-$  facilitates the dissociation of salt, thereby promoting the hydration of  $\text{Fe}^{2+/3+}$  as  $[\text{Fe}(\text{H}_2\text{O})_6]^{2+/3+}$ . Subsequently, six different nitrile solvents were introduced into high-concentration  $\text{Fe}^{2+/3+}$  solu-

tion to further adjust the solvation shell of  $\text{Fe}^{2+/3+}$ , in which the highest  $\alpha$  reached  $3.73 \text{ mV K}^{-1}$  by acetonitrile (MeCN) (low  $c_p \sim 1.75 \text{ J g}^{-1} \text{ K}^{-1}$ ). Spectral characterization combined with molecular dynamics (MD) simulations revealed that nitrile solvents preferentially rearrange the solvent dipole orientation around  $\text{Fe}^{2+}$ , significantly enhancing  $\Delta S$ . The optimal  $\text{Fe}^{2+/3+}$  concentration and MeCN content were systematically investigated to improve the maximum net cooling power from 28.0 to  $48.6 \text{ mW cm}^{-2}$ . Thus, this provided evidence that a COP of 14.3 could someday be achieved in a full system. Furthermore, a demonstration of the cooling effect was operated, generating a peak temperature drop of 1.42 K in the electrolyte. This work provides an effective guiding principle for designing electrolytes for electrochemical refrigeration.

## RESULTS

### Cooling mechanism and electrolyte design principle

The schematics of the Brayton-like thermogalvanic system for electrochemical refrigeration is depicted in Figure 1A, which consists of four essential components: an endothermic reaction half cell, an exothermic reaction half cell, a heat sink, and a heat source. A porous separator connects these two half cells and suppresses the heat transfer. When powered,  $\text{Fe}^{3+}$  in the cathode half cell accepts electrons and reduces to  $\text{Fe}^{2+}$  (cathode), while the reverse oxidation reaction happens on the counter electrode (anode). Note that the more compact solvation shell of  $\text{Fe}^{3+}$  compared with  $\text{Fe}^{2+}$ , due to its higher charge density, gives the  $\Delta S$  a positive value.<sup>23</sup> This reduction reaction with positive  $\Delta S$  is endothermic, which can produce a cooling effect, and companies with exothermic oxidation reaction to pump the heat. Such electrical-driven reversible redox reaction with ions cycling in the electrolyte enables direct and continuous refrigeration. As illustrated in the temperature-entropy diagram (Figure 1B), during step 1-2, the electrolyte undergoes an endothermic reaction in the cathode chamber. The electrolyte will generate cooling power proportional to the product of the  $\Delta S$  and the volume-averaged temperature, while both  $\Delta S$  and  $c_p$  codetermined the actual temperature drop for the electrolyte. In step 2-3, the electrolyte absorbs heat through heat source, increasing its entropy and temperature. In step 3-4, the electrolyte undergoes an exothermic reaction and releases heating energy. The electrolyte will dissipate heat through the heat sink, then be cooled to  $T_c$  and return to its initial state of step 4-1. Obviously, both a large  $\Delta S$  (namely  $\alpha$ ) and low  $c_p$  for electrolytes are essential for efficient electrochemical refrigeration.

The value of  $\alpha$  for thermogalvanic electrolytes is closely related not only to the thermogalvanic ions themselves but also to their surrounding counterions and solvents. The large  $\text{ClO}_4^-$ , characterized by a low charge density and regarded as the structure-breaking ion,<sup>42,43</sup> exhibits weak interactions with both  $\text{Fe}^{2+}$  and  $\text{Fe}^{3+}$ , which can eliminate the undesirable dependence of  $\alpha$  on counterions (Figure S1). To validate this, the aqueous perchlorate solution of  $\text{Fe}^{2+/3+}$  was employed as the “aqueous electrolyte,” which exhibited  $\alpha$  of  $1.73 \text{ mV K}^{-1}$  (Figure 1C). This value is consistent with the ideal  $\Delta S$  for  $[\text{Fe}(\text{H}_2\text{O})_6]^{2+/3+}$  cations,<sup>33,36</sup> suggesting the  $\text{Fe}^{2+/3+}$  mostly coordinated with six water molecules rather than  $\text{ClO}_4^-$ . To further boost the above  $\alpha$ , a rational design of solvent components is essential. The ideal solvent beyond water is

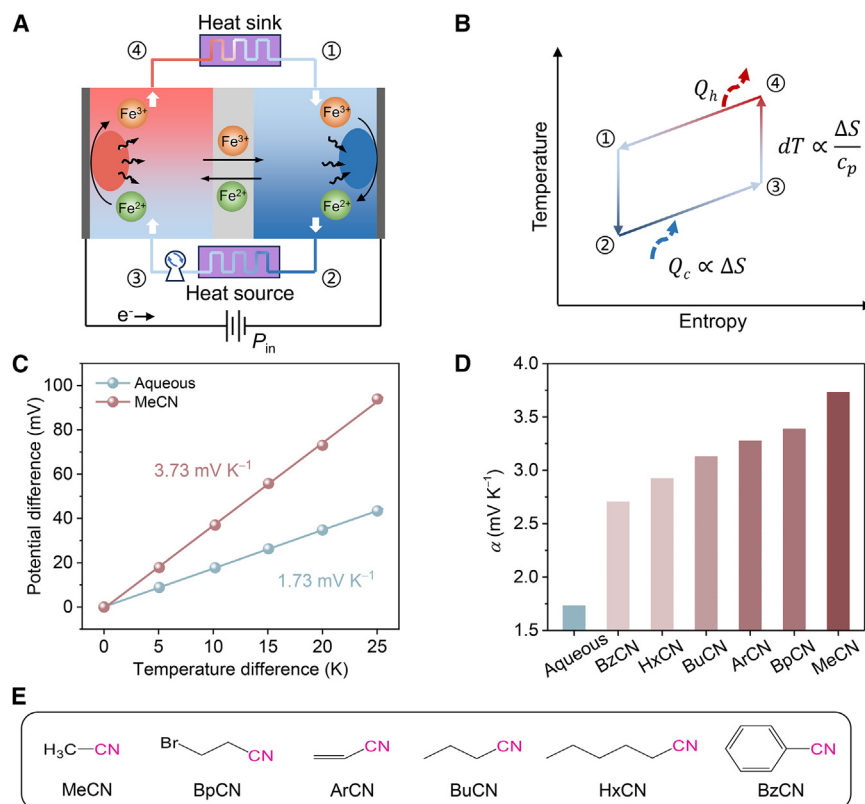


**Figure 1. Cooling mechanism and improvement of temperature coefficient for  $\text{Fe}^{2+/3+}$  electrolyte**

(A) Schematics of a thermogalvanic system using  $\text{Fe}^{2+/3+}$  electrolyte for electrochemical refrigeration. The blue oval represents the endothermic reaction, while the red oval represents the exothermic one. The gray rectangle represents the porous separator that suppresses the heat transfer. The circulation of the electrolyte is driven by the pump.

(B) Corresponding temperature-entropy diagram. The cooling energy ( $Q_c$ ) is proportional to the entropy change of redox reaction ( $\Delta S$ ). Besides, the temperature drop ( $dT$ ) is also determined by the specific heat capacity ( $c_p$ ).

(C) Potential difference versus temperature difference for  $\text{Fe}^{2+/3+}$  electrolyte using pure water (aqueous) and pure acetonitrile (MeCN) as solvents, respectively. Corresponding temperature coefficients ( $\alpha$ ) were calculated from the slope of curves.

(D) Comparison of the  $\alpha$  for  $\text{Fe}^{2+/3+}$  electrolyte using water and six nitriles as solvents, respectively. The solvents used in the above experiment were pure nitriles, and the concentration of  $\text{Fe}^{2+/3+}$  was 0.1 M. Although some nitriles have low solubility in water, they can well dissolve  $\text{Fe}^{2+/3+}$  perchlorate (see also Figure S2).

(E) The chemical structure of the above six nitriles and corresponding abbreviations.

expected to have sufficient interactions with  $\text{Fe}^{2+/3+}$  and thus could compete with water molecules and adjust the solvation shells of  $\text{Fe}^{2+/3+}$  for a larger  $\Delta S$ . Considering the different hardness of  $\text{Fe}^{2+}$  and  $\text{Fe}^{3+}$  as Lewis acids, nitrile solvents were chosen to introduce into the aqueous electrolyte. Nitrile solvents have the soft Lewis basic nature and would preferentially coordinate with softer cations.<sup>44</sup> Six typical nitrile solvents were investigated (Figure 1E): MeCN, benzonitrile (BzCN), hexanenitrile (HxCN), butyronitrile (BuCN), acrylonitrile (ArCN), and 3-bromopropionitrile (BpCN). Remarkably, all these nitriles significantly improved the values of  $\alpha$ , reaching above  $2.7 \text{ mV K}^{-1}$  (Figures 1D and S2). The magnitude order of  $\alpha$  among these nitriles may be explained by their polarity strength (Table S1), which stems from the difference in organic groups (R-CN). Particularly, MeCN, with relatively high polarity, enabled the highest  $\alpha$  of  $3.73 \text{ mV K}^{-1}$ , which surpassed twice the pristine  $\alpha$ . Our strategy also performed best among the existing approaches for optimizing  $\text{Fe}^{2+/3+}$  electrolytes (Table S2). Such great enhancement of  $\alpha$  highlights that nitrile solvents can enlarge the difference between the solvation shells of  $\text{Fe}^{2+}$  and  $\text{Fe}^{3+}$ .

### Investigation of optimizing mechanism of temperature coefficient

To reveal the mechanism underlying the enhanced  $\alpha$  achieved by synergistic effects of  $\text{ClO}_4^-$  counterion and nitrile solvents, ultra-violet-visible (UV-vis) absorption spectroscopy was employed to examine the change in solvation shells of  $\text{Fe}^{2+}$  and  $\text{Fe}^{3+}$ . For the pristine aqueous perchlorate electrolyte, both  $\text{Fe}^{2+}$  and  $\text{Fe}^{3+}$

have a sharp absorption peak at 240 nm (Figure S3), which corresponds to the characteristic absorption of  $[\text{Fe}(\text{H}_2\text{O})_6]^{2+/3+}$  cations.<sup>45,46</sup> Besides, there are not any other absorption peaks observed, confirming the negligible presence of  $\text{Fe}^{2+/3+}-\text{ClO}_4^-$  ion pairs. Thus, the  $\alpha$  of  $\text{Fe}^{2+/3+}$  with  $\text{ClO}_4^-$  as counterion is mainly dominated by the solvents in their solvation shells. Then, the MeCN solvent was added to the perchlorate solution of  $\text{Fe}^{2+}$  and  $\text{Fe}^{3+}$ , respectively. With the increase of MeCN content, the absorption peak of  $\text{Fe}^{2+}$  gradually shifted to a higher wavelength accompanied by an enhanced absorbance (Figure 2A). This change suggests the rearrangement of water molecules in the solvation shell of  $\text{Fe}^{2+}$  due to the presence of MeCN. By contrast, the addition of MeCN had a weak influence on the pristine solvation shell of  $\text{Fe}^{3+}$ , even with pure MeCN as solvent (Figure 2B). This contrasting behavior highlights the selective alteration of the solvation shell for  $\text{Fe}^{2+}$  in a binary solvent of MeCN and water.

To further verify the unique impact of nitrile solvents on the  $\text{Fe}^{2+}$  solvation shell, Raman spectroscopy was chosen due to its high sensitivity toward the  $\text{C}\equiv\text{N}$  vibration. In the binary solvent of MeCN and water, there are two separated peaks for MeCN at around 2,262 and 2,300  $\text{cm}^{-1}$  (Figures 2C and 2D), originating from the  $\text{C}\equiv\text{N}$  stretching and the  $\text{C}-\text{C}\equiv\text{N}$  bending, respectively.<sup>47</sup> Notably, the frequency of  $\text{C}\equiv\text{N}$  vibration is highly sensitive to the strength of interaction with surrounding water molecules or ions.<sup>43</sup> With the  $\text{Fe}^{2+}$  concentration increasing from 0 to 1.6 M, an obvious negative shift in  $\text{C}\equiv\text{N}$  vibration frequency was observed with extra characteristic peaks appearing

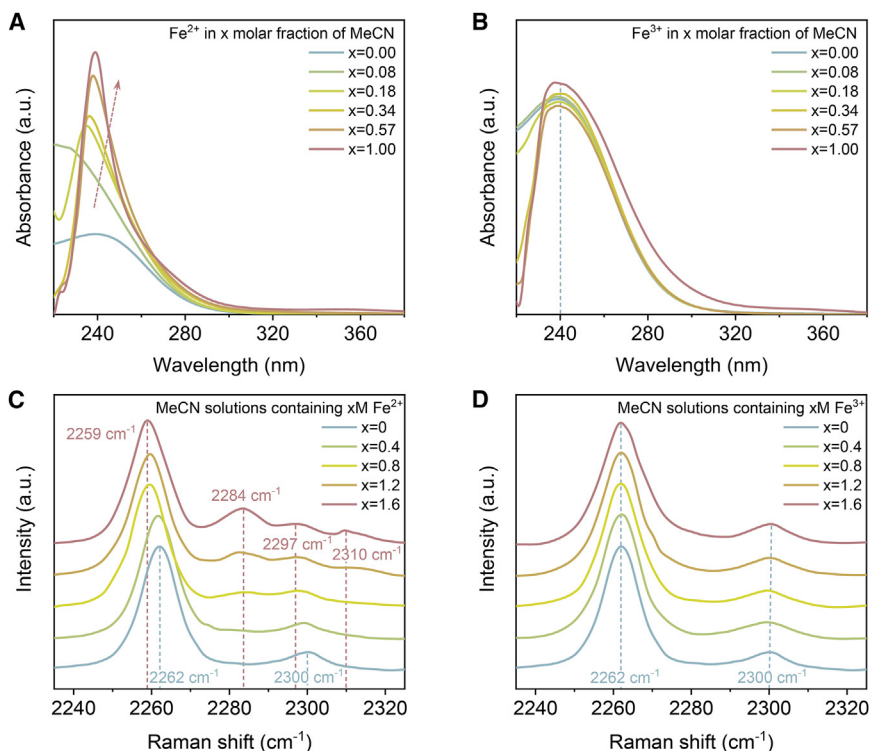


**Figure 2. Characterization of the optimizing mechanism by MeCN**

(A and B) UV-vis spectra for Fe<sup>2+</sup> (A) and Fe<sup>3+</sup> (B) electrolytes with various MeCN contents. The sharp absorption peak at 240 nm corresponded to [Fe(H<sub>2</sub>O)<sub>6</sub>]<sup>2+/3+</sup> hydrated state,<sup>45,46</sup> and the change of the characteristic peaks was marked by the dashed lines.

(C and D) Raman spectra for MeCN solutions containing various concentrations of Fe<sup>2+</sup> (C) and Fe<sup>3+</sup> (D). The characteristic peaks of MeCN located around 2,262 and 2,300 cm<sup>-1</sup>, and their change and the appearance of new peaks were marked by the dashed lines. The above spectra identified that MeCN selectively interacted with Fe<sup>2+</sup> compared with Fe<sup>3+</sup> and adjusted its solvation shell.

around 2,284 and 2,310 cm<sup>-1</sup> (Figure 2C), reflecting the diverse interactions of MeCN with water molecules and Fe<sup>2+</sup>. By contrast, the C≡N vibration frequency of MeCN remained nearly unchanged in high-concentration Fe<sup>3+</sup> aqueous solution compared with the pristine value (Figure 2D). This distinct behavior was consistently observed for the other five nitriles with Fe<sup>2+</sup> and Fe<sup>3+</sup>, respectively (Figure S4). These results demonstrate that nitrile solvents have much stronger interactions with Fe<sup>2+</sup> than Fe<sup>3+</sup>, leading to the adjustment of the solvation shell toward a larger entropy difference (namely higher  $\alpha$ ).

To illuminate the detailed evolution of the solvent shell, MD simulation was employed to monitor the dissolution environment of Fe<sup>2+/3+</sup> in both unary and binary solvents (Notes S2 and S3; Table S3). The diffusion coefficients and densities suggested the reliability of our force field parameters (Table S4). Notably, experimental findings demonstrated that a significant increase in  $\alpha$  was observed up to a MeCN:H<sub>2</sub>O ratio of 1:2 (Figure S6). Consequently, our primary focus was directed toward investigating the MeCN effect on the solvation shell with the molar ratio of MeCN:H<sub>2</sub>O (1:2 for system 2). The radial density profile and the coordination number distribution of water molecules for the Fe<sup>2+/3+</sup> were analyzed in Figures 3B and S7. The first peak of water number density distribution ( $\rho_{\text{water}}$ ) for Fe<sup>3+</sup> located at 2.06 Å, while a larger value of 2.16 Å for Fe<sup>2+</sup>. Indeed, the Fe<sup>3+</sup> with relatively higher valence enables a more closely packed solvation shell. The radius of the first solvation shell can be obtained by the first minimum in the radial distribution functions.<sup>48</sup> Thus, the coordination number of water molecules in the first solvation shell for both Fe<sup>2+</sup> and Fe<sup>3+</sup> is determined as 6 (Figure S7), which is consistent with the hydrated state [Fe(H<sub>2</sub>O)<sub>6</sub>]<sup>2+/3+</sup> confirmed

by the UV-vis spectrum (Figure S3). When MeCN was introduced, a clear peak of MeCN number density distribution ( $\rho_{\text{MeCN}}$ ) for Fe<sup>2+</sup> appeared at 5.54 Å, while there was no significant peak for Fe<sup>3+</sup> (Figure 3C). Similar phenomena were observed in binary solvents with various molar ratios of MeCN:H<sub>2</sub>O (Figure S8). Meanwhile, the introduction of MeCN generated a larger change to the

water molecule distribution in the solvation shell of Fe<sup>2+</sup> than Fe<sup>3+</sup> (Figures S7 and S9). These phenomena illustrate that MeCN indeed selectively participates in the solvation shell of Fe<sup>2+</sup> (Figure 3A), which may increase the solvation entropy difference between Fe<sup>2+</sup> and Fe<sup>3+</sup>. To further bridge the change of solvation shell to the solvation entropy and  $\alpha$ , the order of solvent molecules was investigated by the probability distribution of dipole orientation (see Note S3 for details). The probability distribution of dipole orientation was characterized by the angle  $\theta$  between the dipole of water and the direction of O (in water) to Fe<sup>2+/3+</sup> (Figure 3D). Apparently, the  $\theta$  exhibited a broader distribution with the addition of MeCN solvent into water. The variance of dipole fluctuation ( $\sigma^2[\theta]$ ) can be used to describe the solvation shell order of an ion, and a higher value means a less ordered solvation shell.<sup>41</sup> The  $\sigma^2[\theta]$  for Fe<sup>2+</sup> largely increased from 57 to 68 with MeCN added, while only a small increase  $\sim 4$  in the  $\sigma^2[\theta]$  for Fe<sup>3+</sup> (Figure S10). Similar phenomena were also observed in binary solvents with various molar ratios of MeCN:H<sub>2</sub>O (Figure S11). Consequently, the difference between the  $\sigma^2[\theta]$  for Fe<sup>2+</sup> and Fe<sup>3+</sup>, named  $\xi_{\text{rxn}}$ , exhibited a notable growth (Figure 3E) with increasing the molar ratio of MeCN:H<sub>2</sub>O (Figure S12). Such change of solvation shell order induced by MeCN explains the increased solvation entropy difference between Fe<sup>2+</sup> and Fe<sup>3+</sup> as well as the highly boosted  $\alpha$ . Furthermore, the temperature-dependent solvation free energy of Fe<sup>2+</sup> and Fe<sup>3+</sup> was calculated to estimate the  $\alpha$  value (Figures 3F and S13). The  $\alpha$  for Fe<sup>2+/3+</sup> in various molar ratios of MeCN:H<sub>2</sub>O was predicted  $\sim 1.87, 2.22, 2.87, 3.13, \text{ and } 3.28 \text{ mV K}^{-1}$ , consistent with our experimental results (Figure S14; Note S3).



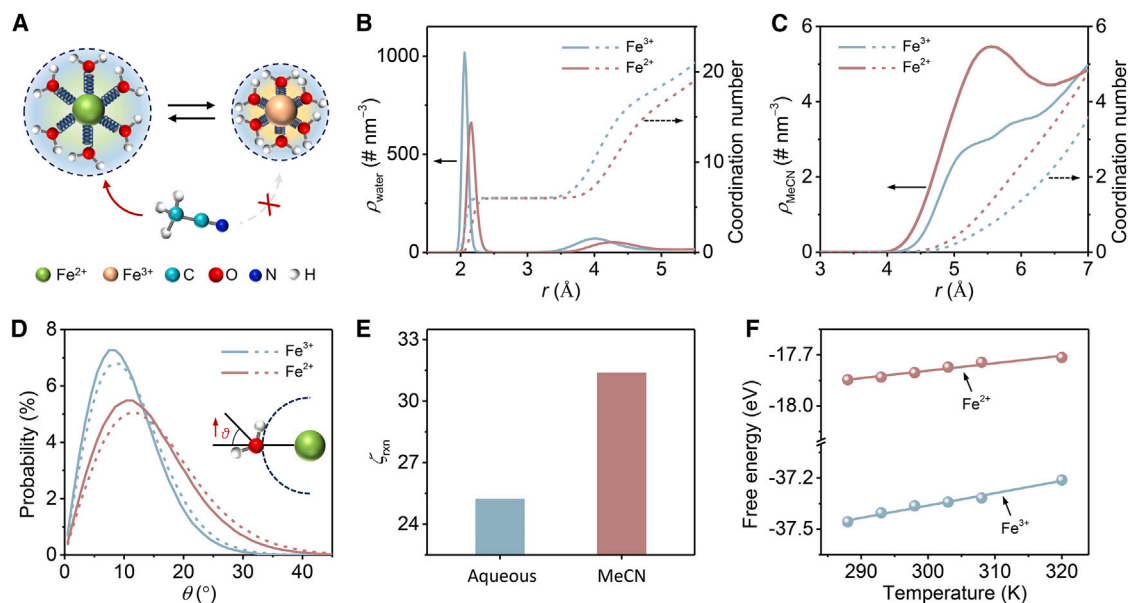


**Figure 3. MD simulation for  $\text{Fe}^{2+/3+}$  electrolyte with added MeCN**

(A) Schematics of the solvation structure of  $\text{Fe}^{2+}$  and  $\text{Fe}^{3+}$ , and the selective interaction of MeCN.

(B and C) Radial density ( $\rho$ ) and coordination number profiles of water (B) and MeCN (C) molecules in the solvation shell of  $\text{Fe}^{2+}$  and  $\text{Fe}^{3+}$ .

(D) Probability distribution of dipole orientation in the solvation shell of  $\text{Fe}^{2+}$  and  $\text{Fe}^{3+}$ . The solid lines denote the aqueous system, while the dashed lines denote the MeCN system. The inset shows the angle  $\theta$  between the dipole of water and the direction of O (in water) to  $\text{Fe}^{2+/3+}$ .

(E)  $\xi_{\text{rn}}$  of  $\text{Fe}^{2+/3+}$  in pure water (aqueous) and with MeCN added, which reflected the entropy difference between  $\text{Fe}^{2+}$  and  $\text{Fe}^{3+}$  and defined as the difference between the variance of dipole fluctuation of them (see also Figure S10).

(F) The solvation energy of  $\text{Fe}^{2+}$  and  $\text{Fe}^{3+}$  with MeCN added at various temperatures. The details for MD simulation and dipole fluctuation calculation were illuminated in Notes S2 and S3.

### Characterization of cooling performance of electrolyte

The excellent  $\alpha$  can generate high theoretical cooling power under a given electrical input (see Note S1 for details). Among nitrile solvents, MeCN-based electrolytes possessed the highest  $\alpha$  and thus were used in the following optimizations of cooling performances. The  $c_p$  is another critical parameter of electrolytes for efficient electrochemical refrigeration.<sup>10,12,20</sup> As the intrinsic high  $c_p$  of water, aqueous electrolytes are undesirable with the limited cooling effect compared with organic refrigerants. Benefiting from the much lower  $c_p$  of MeCN, the average  $c_p$  of MeCN/ $\text{H}_2\text{O}$ -based electrolytes near ambient temperature (283–318 K) remarkably decreased from 3.80 to 1.75  $\text{J g}^{-1} \text{K}^{-1}$  (Figure 4A). In a comprehensive comparison with current thermogalvanic electrolytes (Figure 4B; Table S5), our electrolytes exhibited the best property with both high  $\alpha$  and low  $c_p$ , laying the foundation for excellent cooling performance.

Although the theoretical cooling power improved by  $\sim 116\%$  (Figure S15), achieving optimal electrolyte-specific cooling power ( $P_{\text{c,e}}$ ) in practice requires balancing the parasitic Joule heat. The Joule heat, stemming from the internal resistance, following an ohmic relationship, determined primarily by the ionic conductivity ( $\sigma$ ) (Figure S16). To obtain the optimum components of  $\text{Fe}^{2+/3+}$  electrolyte based on MeCN/ $\text{H}_2\text{O}$ , the power factor ( $PF = \sigma\alpha^2$ ) was used as the screening criterion (Figures S17 and S18; Note S6). The binary solvent with a molar ratio of 1.9:1 between MeCN and  $\text{H}_2\text{O}$ , and a relatively high  $\text{Fe}^{2+/3+}$  concentration (0.4 M), exhibited the largest  $PF$  of 35.8  $\mu\text{W m}^{-1} \text{K}^{-2}$

and moderate stability (Figure S19). As a result, in practical refrigeration operations (see methods for details), the  $P_{\text{c,e}}$  for such an optimized electrolyte was remarkably boosted as high as 48.6  $\text{mW cm}^{-2}$  under a voltage input ( $V_{\text{in}}$ ) of 0.8 V from pristine 28.0  $\text{mW cm}^{-2}$  (Figure 4C). The decrease of  $P_{\text{c,e}}$  under higher  $V_{\text{in}}$  is caused by the square increase of Joule heat, while the optimized electrolyte can remain at a much higher  $P_{\text{c,e}}$ . Furthermore, the corresponding electrolyte-specific COP ( $\text{COP}_\text{e}$ ) was calculated based on the  $P_{\text{c,e}}$  and electrical input (Figure 4D; Note S1). The  $\text{COP}_\text{e}$  value for the maximum  $P_{\text{c,e}}$  is 0.74, which is twice the pristine value (0.37). Under a lower  $V_{\text{in}}$ , the  $\text{COP}_\text{e}$  could achieve values of 14.3, meaning it is possible to achieve high cooling efficiency and potential compatibility with emerging microenergy technologies. Toward real-world application, further development of matching evaporators, condenser heat exchangers, and internal heat recuperators is needed in the future, and the system cycle life is also essential to be considered.

### Demonstration and analysis of practical cooling effect

To demonstrate the practical cooling effect for the optimized thermogalvanic electrolyte, a sandwich-like electrochemical reactor was designed (Figure S20). The  $\text{Fe}^{2+/3+}$  electrolyte is injected into two chambers filled with commercial carbon felt electrodes and separated by the porous medium. In continuous refrigeration, a part of electrolyte is cooled in the cathode chamber and pumped out for use; meanwhile, another part brings out the heat from the anode chamber. The temperature of electrolyte

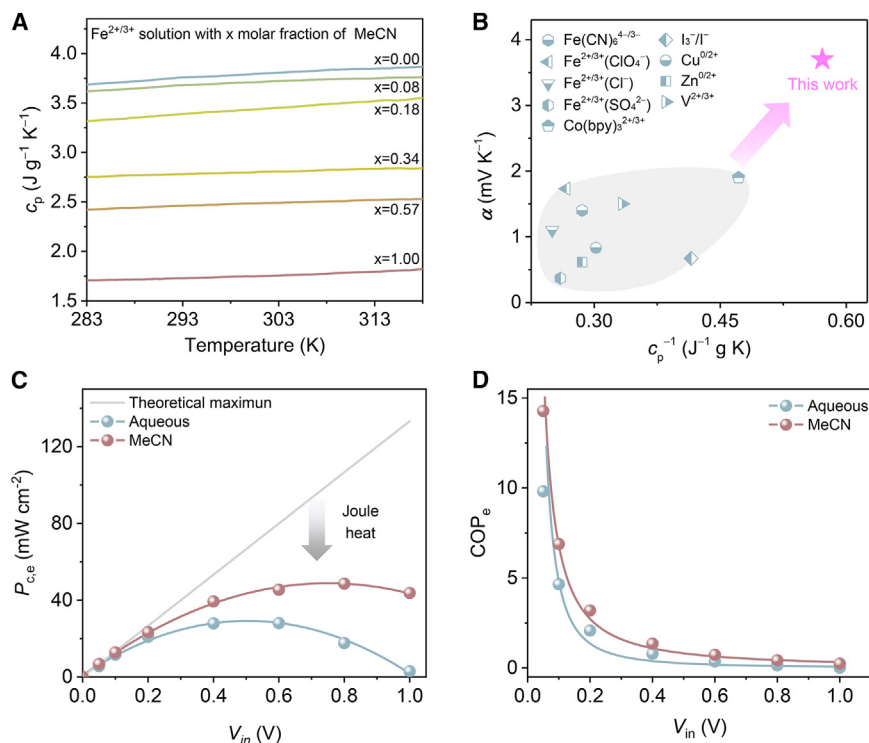


**Figure 4. Cooling performance of  $\text{Fe}^{2+/3+}$  electrolyte with added MeCN**

(A) The specific heat capacity ( $c_p$ ) versus temperature for  $\text{Fe}^{2+/3+}$  electrolyte with various MeCN contents.

(B) Comparison of the  $\alpha$  and  $c_p^{-1}$  for some typical thermogalvanic electrolytes (Table S5). Both high  $\alpha$  and low  $c_p$  are crucial to efficient electrochemical refrigeration, and our optimized electrolyte performs best.

(C and D) The electrolyte-specific cooling power (C) and electrolyte-specific COP (D) at various voltage inputs ( $V_{in}$ ) for the pristine electrolyte (aqueous) and optimized electrolyte (MeCN). Note that the deviation of net cooling power from the linear theoretical value is caused by the Joule heat, especially large for high  $V_{in}$ .

## DISCUSSION

In summary, this work developed a design strategy for thermogalvanic electrolytes for efficient electrochemical refrigeration by solvation entropy engineering. By introducing  $\text{ClO}_4^-$  as a counterion and nitriles as co-solvents into aqueous  $\text{Fe}^{2+/3+}$  electrolytes together,

in each chamber was recorded, and the temperature change in the cathode chamber was regarded as the effective temperature drop (Figures S21 and S22). The use of the optimized electrolyte exhibited a doubled stable temperature drop under each  $V_{in}$  compared with the pristine electrolyte (Figures 5A and 5B). The maximum stable temperature drop of our electrolyte reached 1.42 K under a  $V_{in}$  of 0.8 V, significantly higher than previous electrolytes, showcasing an orders-of-magnitude improvement in both cooling power and COP (Figure S23).<sup>10–12</sup> Moreover, a static device based on isothermal cycle,<sup>12</sup> designed to visually demonstrate the cooling effect (Figure 5C), shows a clear cooling effect in the cathode area (Figure 5D; Video S1).

Since the practical refrigerant is achieved by heat transfer between the electrolyte and the cooling target, the electrochemical refrigeration is eager for a higher temperature drop. Under constant voltage input, the cooling effect is proportional to the extent of the reaction, which can be evaluated by the concentration of the flowing electrolyte participating in the reaction (defined as  $c_{\text{eff}}$ ). According to our calculation (Note S4), the  $c_{\text{eff}}$  for 1.42 K is 0.078 M, much lower than the concentration of the electrolyte (0.4 M). Therefore, increasing  $c_{\text{eff}}$  with constant input voltage could potentially achieve a higher temperature drop. Based on the essential parameters (Figures 4A, S18, and S24), the electrochemical refrigeration system is expected to reach a prospective temperature drop with over 0.19 M effective  $\text{Fe}^{2+/3+}$  (Figure S25; Note S4). Studies have shown that electrodes with higher catalytic activity and larger specific surface areas can facilitate the reaction.<sup>49–51</sup> Prospectively, combining our electrolyte with advanced electrodes to improve effective redox concentrations is hopeful to further activate the great cooling potential of thermogalvanic systems.

both the  $\alpha$  and  $c_p$  were remarkably optimized, outperforming the reported thermogalvanic electrolytes. The combination of spectroscopy and MD simulation revealed the weak  $\text{Fe}^{2+/3+}-\text{ClO}_4^-$  interaction and selective association between  $\text{Fe}^{2+}$  and nitriles, leading to a synergistic adjustment of the solvation shell components and the dipole orientation. Especially, the different change in the solvation shell order of  $\text{Fe}^{2+}$  and  $\text{Fe}^{3+}$  directly enlarged their solvation entropy difference and thus boosted the  $\alpha$ . With further optimizations of  $\text{Fe}^{2+/3+}$  concentration and MeCN content, the cooling power improved  $\sim 70\%$ , and it is possible to achieve a COP<sub>e</sub> of 14.3. Moreover, the practical cooling effect was demonstrated with a considerable temperature drop of electrolyte of  $\sim 1.42$  K with only  $0.11 \text{ W cm}^{-2}$  input. Prospectively, our electrolyte design principle based on solvation entropy engineering could be effective for not only electrochemical refrigeration but also broader thermogalvanic energy conversion technologies.

## METHODS

### Materials

Iron(III) perchlorate hydrate was purchased from Sigma-Aldrich. Methyl cyanide was purchased from Shanghai Macklin Biochemical Technology. Iron(II) perchlorate hydrate, perchloric acid, BzCN, HxCN, BuCN, ArCN, and 3-bromopropyronitrile were purchased from Shanghai Aladdin Biochemical Technology. All chemical reagents were used without further purification. Graphite sheets were purchased from Shanghai CARBON. Carbon felt and carbon cloth were purchased from Jingzhou Haote New Material. The deionized (DI) water used in all experiments was purified using a Simplicity Milli-Q system (Millipore, France).

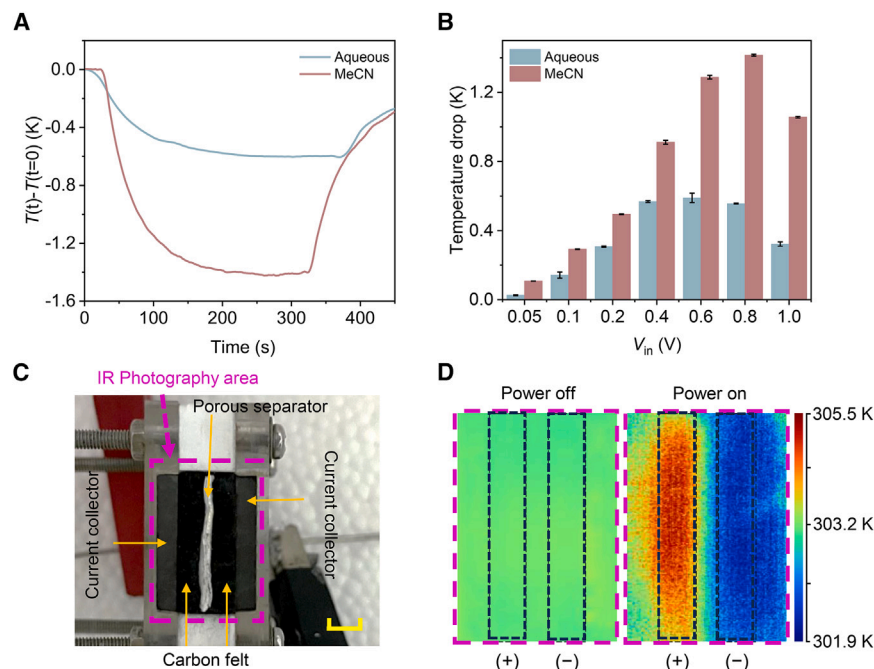


**Figure 5. Demonstration of the practical cooling effect**

(A) The real-time maximum temperature drop ( $T(t) - T(t = 0)$ ) profiles for pristine electrolyte (aqueous) and optimized electrolyte (MeCN).

(B) Comparison of the stable temperature drop generated with various voltage inputs ( $V_{in}$ ) for the pristine electrolyte and optimized electrolyte. Data are represented as mean  $\pm$  SEM.

(C) Photograph of the static device (based on isothermal cycle), which was designed to visually demonstrate the cooling effect. The yellow scale bar represents 5 mm.

(D) Infrared photograph of the cross-section of the static device before (left) and after (right) power on, showing a clear cooling effect. The area of infrared photograph and electrolyte was marked by purple and black dashed box, respectively.

### Mechanism characterization

The interaction between nitriles and  $\text{Fe}^{2+/3+}$  was characterized with a UV-vis-NIR spectrometer (UV-3600 plus, Shimadzu) and a laser confocal Raman spectrometer (LabRAM HR800, Horiba Jobin Yvon). For UV-vis characterization, the loading buffer was diluted to meet the upper limit of the spectrometer. For Raman characterization, a 532 nm laser extinction was chosen because it has relatively high sensitivity and can collect the spectra in the range of 100–4,000  $\text{cm}^{-1}$ , which covers the Raman characteristic area of nitriles. The container for our liquid was a capillary tube. The laser was focused on the liquid phase to obtain characteristic signals of the liquid. The content of nitrile solvents was maintained at 5 mol % for each sample. For these nitriles undissolved with water, methanol was used to replace water as a co-solvent because methanol had no obvious signal in the Raman characteristic area of nitriles and had a negligible effect on the solvent structure of  $\text{Fe}^{2+/3+}$  (Figures S4A and S5; Note S5).

### MD preparation

MD simulations were performed using the GROMACS<sup>52</sup> MD package. Water molecules were modeled with the extended simple point charge model (SPC/E) framework,<sup>53</sup> and the Lennard-Jones parameters for  $\text{Fe}^{3+}/\text{Fe}^{2+}$  ions were derived by Aguilar et al.<sup>54</sup> The optimized potentials for liquid simulations (OPLS) force field was applied to model the  $\text{ClO}_4^-$  anion and MeCN solvent.<sup>55</sup> A detailed summary of the simulation setup, including the number of cations, anions, water molecules, and MeCN molecules for each system, is provided in Table S3. Additional details are available in Note S2. The solvation entropy was analyzed in terms of the type, quantity, and arrangement of solvent molecules, as well as the probability distribution of dipole orientations. Further insights are provided in Note S3.

### Performance characterization

The voltage and current profiles were measured with a Keithley 2400 instrument, which served as a constant voltage source for the cooling performance tests.

The corresponding temperature profiles

were recorded by a thermocouple data logger (USB-TC-08, Pico Technology, St. Neots, UK). The curves of the potential difference at various temperature differences were obtained, and the temperature coefficient was calculated by the slopes of these curves. The specific heat capacity was measured with a differential scanning calorimeter (Diamond DSC, PerkinElmer Instruments). The electrical conductivity was measured with a conductivity meter (SevenCompact S230, Mettler Toledo). The infrared images and video were taken by a thermal imager (TiX520, Fluke). In thermogalvanic and cooling performance tests, the initial working temperature was controlled at around 298 K.

### Device preparation and operation

The device used to test the cooling performance was a typical sandwich-like cell made of poly(methyl methacrylate) frame. Two graphite sheets were fixed at each side as current collectors with an internal distance of 4 mm. The internal chamber was divided into two half cells by a porous separator and filled with carbon cloth as the electrode. The cross-sectional area of electrode was 0.7  $\text{cm}^2$  (1.4 cm  $\times$  0.5 cm). The thermocouple was touched with each electrode to monitor the temperature. For continuous refrigeration (Figure S20), the electrolyte was flowed through each half cell with a constant rate of 0.8  $\text{mL min}^{-1}$  by a multi-channel peristaltic pump (BT100L, Leadfluid). For the static refrigeration device, the distance of graphite sheets was 8 mm (the carbon felts with the thickness of 3 mm and the porous separator with the thickness of 2 mm). The cross-sectional area of electrode was 2  $\text{cm}^2$  (2 cm  $\times$  1 cm). The carbon felts were highly packed, and each of them could hold 0.12 mL of solution. The constant voltage was applied to the device by a Keithley 2400 instrument for driving refrigeration.



## RESOURCE AVAILABILITY

## Lead contact

Further information and requests for resources should be directed to and will be fulfilled by the lead contact, Jiangjiang Duan ([jiangjiangduan@hust.edu.cn](mailto:jiangjiangduan@hust.edu.cn)).

## Materials availability

This study did not generate new unique materials.

## Data and code availability

All relevant data that support the findings of this study are presented in the manuscript and [supplemental information](#) file. There is no code used in this study. Source data are available from the corresponding author upon reasonable request.

## ACKNOWLEDGMENTS

This work was supported by the National Natural Science Foundation of China (52272204, 52002139, 52106090, 62161160311, T2325012) and the China National Postdoctoral Program for Innovative Talents (BX20240363). The authors thank the Center for Nanoscale Characterization & Devices, WNLO-HUST, and the Analysis and Testing Center of Huazhong University of Science and Technology for their support. This manuscript is dedicated to the memory of Prof. Jun Zhou.

## AUTHOR CONTRIBUTIONS

J.D. and B.Y. conceived and designed the project. J.D. and G.F. supervised the project. Y.Z. and B.Y. carried out the experiments. M.C., J. Zhang, and G.F. carried out the MD simulations. Y.Z., B.Y., M.C., P.L., J.G., J.W., and J.D. analyzed the data. B.Y., Y.Z., J.D., M.C., and G.F. wrote the paper. All authors discussed the results and approved the final version of the manuscript.

## DECLARATION OF INTERESTS

The authors declare no competing interests.

## SUPPLEMENTAL INFORMATION

Supplemental information can be found online at <https://doi.org/10.1016/j.joule.2025.101822>.

Received: October 29, 2024

Revised: December 14, 2024

Accepted: January 2, 2025

Published: January 30, 2025

## REFERENCES

- Sherwood, S.C. (2020). Adapting to the challenges of warming. *Science* 370, 782–783. <https://doi.org/10.1126/science.abe4479>.
- Grocholski, B. (2020). Cooling in a warming world. *Science* 370, 776–777. <https://doi.org/10.1126/science.abf1931>.
- Poredoš, P., and Wang, R. (2023). Sustainable cooling with water generation. *Science* 380, 458–459. <https://doi.org/10.1126/science.add1795>.
- McLinden, M.O., Brown, J.S., Brignoli, R., Kazakov, A.F., and Domanski, P.A. (2017). Limited options for low-global-warming-potential refrigerants. *Nat. Commun.* 8, 14476. <https://doi.org/10.1038/ncomms14476>.
- McLinden, M.O., Seaton, C.J., and Pearson, A. (2020). New refrigerants and system configurations for vapor-compression refrigeration. *Science* 370, 791–796. <https://doi.org/10.1126/science.abe3692>.
- Mao, J., Chen, G., and Ren, Z. (2021). Thermoelectric cooling materials. *Nat. Mater.* 20, 454–461. <https://doi.org/10.1038/s41563-020-00852-w>.
- Qin, B., Wang, D., Liu, X., Qin, Y., Dong, J.F., Luo, J., Li, J.W., Liu, W., Tan, G., Tang, X., et al. (2021). Power generation and thermoelectric cooling enabled by momentum and energy multiband alignments. *Science* 373, 556–561. <https://doi.org/10.1126/science.abi8668>.
- Hou, H., Qian, S., and Takeuchi, I. (2022). Materials, physics and systems for multicaloric cooling. *Nat. Rev. Mater.* 7, 633–652. <https://doi.org/10.1038/s41578-022-00428-x>.
- Lilley, D., and Prasher, R. (2022). Ionocaloric refrigeration cycle. *Science* 378, 1344–1348. <https://doi.org/10.1126/science.ade1696>.
- Rajan, A., McKay, I.S., and Yee, S.K. (2022). Continuous electrochemical refrigeration based on the Brayton cycle. *Nat. Energy* 7, 320–328. <https://doi.org/10.1038/s41560-021-00975-7>.
- Zhou, H., Matoba, F., Matsuno, R., Wakayama, Y., and Yamada, T. (2023). Direct conversion of phase-transition entropy into electrochemical thermopower and the Peltier effect. *Adv. Mater.* 35, e2303341. <https://doi.org/10.1002/adma.202303341>.
- McKay, I.S., Kunz, L.Y., and Majumdar, A. (2019). Electrochemical redox refrigeration. *Sci. Rep.* 9, 13945. <https://doi.org/10.1038/s41598-019-50118-y>.
- Liu, Y., Cui, M., Ling, W., Cheng, L., Lei, H., Li, W., and Huang, Y. (2022). Thermo-electrochemical cells for heat to electricity conversion: from mechanisms, materials, strategies to applications. *Energy Environ. Sci.* 15, 3670–3687. <https://doi.org/10.1039/d2ee01457b>.
- Liu, Y., Wang, H., Sherrell, P.C., Liu, L., Wang, Y., and Chen, J. (2021). Potentially wearable thermo-electrochemical cells for body heat harvesting: from mechanism, materials, strategies to applications. *Adv. Sci.* 8, 2100669. <https://doi.org/10.1002/advs.202100669>.
- He, X., Sun, H., Li, Z., Chen, X., Wang, Z., Niu, Y., Jiang, J., and Wang, C. (2022). Redox-induced thermocells for low-grade heat harvesting: mechanism, progress, and their applications. *J. Mater. Chem. A* 10, 20730–20755. <https://doi.org/10.1039/d2ta05742e>.
- Zhang, J., Shao, D., Jiang, L., Zhang, G., Wu, H., Day, R., and Jiang, W. (2022). Advanced thermal management system driven by phase change materials for power lithium-ion batteries: a review. *Renew. Sustain. Energy Rev.* 159, 112207. <https://doi.org/10.1016/j.rser.2022.112207>.
- Habibi Khalaj, A., and Halgamuge, S.K. (2017). A review on efficient thermal management of air- and liquid-cooled data centers: from chip to the cooling system. *Appl. Energy* 205, 1165–1188. <https://doi.org/10.1016/j.apenergy.2017.08.037>.
- Gerlach, D.W., and Newell, T.A. (2007). Basic modelling of direct electrochemical cooling. *Int. J. Energy Res.* 31, 439–454. <https://doi.org/10.1002/er.1250>.
- Duan, Z.N., Qu, Z.G., and Zhang, J.F. (2021). Thermodynamic and electrochemical performance analysis for an electrochemical refrigeration system based on iron/vanadium redox couples. *Electrochim. Acta* 389, 138675. <https://doi.org/10.1016/j.electacta.2021.138675>.
- Rajan, A., and Yee, S.K. (2022). System dynamics and metrics of an electrochemical refrigerator based on the Brayton cycle. *Cell Rep. Phys. Sci.* 3, 100774. <https://doi.org/10.1016/j.xcrp.2022.100774>.
- Duan, J., Yu, B., Huang, L., Hu, B., Xu, M., Feng, G., and Zhou, J. (2021). Liquid-state thermocells: opportunities and challenges for low-grade heat harvesting. *Joule* 5, 768–779. <https://doi.org/10.1016/j.joule.2021.02.009>.
- Yu, B., and Duan, J. (2023). Electrochemical waste-heat harvesting. *Science* 381, 269–270. <https://doi.org/10.1126/science.adi8036>.
- Li, W., Ma, J., Qiu, J., and Wang, S. (2022). Thermocells-enabled low-grade heat harvesting: challenge, progress, and prospects. *Mater. Today Energy* 27, 101032. <https://doi.org/10.1016/j.mtener.2022.101032>.
- Yu, B., Duan, J., Cong, H., Xie, W., Liu, R., Zhuang, X., Wang, H., Qi, B., Xu, M., Wang, Z.L., et al. (2020). Thermosensitive crystallization-boosted liquid thermocells for low-grade heat harvesting. *Science* 370, 342–346. <https://doi.org/10.1126/science.abd6749>.
- Han, C.G., Qian, X., Li, Q., Deng, B., Zhu, Y., Han, Z., Zhang, W., Wang, W., Feng, S.P., Chen, G., et al. (2020). Giant thermopower of ionic gelatin near room temperature. *Science* 368, 1091–1098. <https://doi.org/10.1126/science.aaz5045>.

26. Wang, Y., Zhang, Y., Xin, X., Yang, J., Wang, M., Wang, R., Guo, P., Huang, W., Sobrido, A.J., Wei, B., et al. (2023). In situ photocatalytically enhanced thermogalvanic cells for electricity and hydrogen production. *Science* 381, 291–296. <https://doi.org/10.1016/j.cjsc.2023.100195>.
27. Lei, Z., Gao, W., and Wu, P. (2021). Double-network thermocells with extraordinary toughness and boosted power density for continuous heat harvesting. *Joule* 5, 2211–2222. <https://doi.org/10.1016/j.joule.2021.06.003>.
28. Duan, J., Feng, G., Yu, B., Li, J., Chen, M., Yang, P., Feng, J., Liu, K., and Zhou, J. (2018). Aqueous thermogalvanic cells with a high Seebeck coefficient for low-grade heat harvest. *Nat. Commun.* 9, 5146. <https://doi.org/10.1038/s41467-018-07625-9>.
29. Liu, L., Zhang, D., Bai, P., Mao, Y., Li, Q., Guo, J., Fang, Y., and Ma, R. (2023). Strong tough thermogalvanic hydrogel thermocell with extraordinarily high thermoelectric performance. *Adv. Mater.* 35, e2300696. <https://doi.org/10.1002/adma.202300696>.
30. Li, J., Chen, S., Han, Z., Qu, X., Jin, M., Deng, L., Liang, Q., Jia, Y., and Wang, H. (2023). High performance bacterial cellulose organogel-based thermoelectrochemical cells by organic solvent-driven crystallization for body heat harvest and self-powered wearable strain sensors. *Adv. Funct. Mater.* 33, 2306509. <https://doi.org/10.1002/adfm.202306509>.
31. Zhang, H., Wang, Z., Li, H., Salla, M., Song, Y., Huang, S., Huang, S., Wang, X., Liu, K., Xu, G., et al. (2023). Continuous electricity generation from solar heat and darkness. *Joule* 7, 1515–1528. <https://doi.org/10.1016/j.joule.2023.06.009>.
32. Buckingham, M.A., Laws, K., Li, H., Kuang, Y., and Aldous, L. (2021). Thermogalvanic cells demonstrate inherent physiochemical limitations in redox-active electrolytes at water-in-salt concentrations. *Physiol. Sci.* 2, 100510. <https://doi.org/10.1016/j.xcrp.2021.100510>.
33. deBethune, A.J., Licht, T.S., and Swendeman, N. (1959). The temperature coefficients of electrode potentials. *J. Electrochem. Soc.* 106, 616–625. <https://doi.org/10.1149/1.2427448>.
34. Kim, T., Lee, J.S., Lee, G., Yoon, H., Yoon, J., Kang, T.J., and Kim, Y.H. (2017). High thermopower of ferri/ferrocyanide redox couple in organic-water solutions. *Nano Energy* 31, 160–167. <https://doi.org/10.1016/j.nanoen.2016.11.014>.
35. Hupp, J.T., and Weaver, M.J. (1984). Solvent, ligand, and ionic charge effects on reaction entropies for simple transition-metal redox couples. *Inorg. Chem.* 23, 3639–3644. <https://doi.org/10.1021/ic00190a042>.
36. Buckingham, M.A., Laws, K., Cross, E., Surman, A.J., and Aldous, L. (2021). Developing iron-based anionic redox couples for thermogalvanic cells: towards the replacement of the ferricyanide/ferrocyanide redox couple. *Green Chem.* 23, 8901–8915. <https://doi.org/10.1039/d1gc02989d>.
37. Buckingham, M.A., Marken, F., and Aldous, L. (2018). The thermoelectrochemistry of the aqueous iron(II)/iron(III) redox couple: significance of the anion and pH in thermogalvanic thermal-to-electrical energy conversion. *Sustainable Energy Fuels* 2, 2717–2726. <https://doi.org/10.1039/c8se00416a>.
38. Yang, P., Liu, K., Chen, Q., Mo, X., Zhou, Y., Li, S., Feng, G., and Zhou, J. (2016). Wearable thermocells based on gel electrolytes for the utilization of body heat. *Angew. Chem. Int. Ed. Engl.* 55, 12050–12053. <https://doi.org/10.1002/anie.201606314>.
39. Inoue, D., Niwa, H., Nitani, H., and Moritomo, Y. (2021). Scaling relation between electrochemical Seebeck coefficient for  $\text{Fe}^{2+}/\text{Fe}^{3+}$  in organic solvent and its viscosity. *J. Phys. Soc. Jpn.* 90, 033602. <https://doi.org/10.7566/JPSJ.90.033602>.
40. Liu, Y., Zhang, Q., Odunmbaku, G.O., He, Y., Zheng, Y., Chen, S., Zhou, Y., Li, J., Li, M., and Sun, K. (2022). Solvent effect on the Seebeck coefficient of  $\text{Fe}^{2+}/\text{Fe}^{3+}$  hydrogel thermogalvanic cells. *J. Mater. Chem. A* 10, 19690–19698. <https://doi.org/10.1039/d1ta10508f>.
41. Chen, Y., Huang, Q., Liu, T.-H., Qian, X., and Yang, R. (2023). Effect of solvation shell structure on thermopower of liquid redox pairs. *Ecomat.* 5, e12385. <https://doi.org/10.1002/eom2.12385>.
42. Marcus, Y. (2009). Effect of ions on the structure of water: structure making and breaking. *Chem. Rev.* 109, 1346–1370. <https://doi.org/10.1021/cr8003828>.
43. Huang, B., Mui, S., Feng, S., Katayama, Y., Lu, Y.C., Chen, G., and Shao-Horn, Y. (2018). Non-covalent interactions in electrochemical reactions and implications in clean energy applications. *Phys. Chem. Chem. Phys.* 20, 15680–15686. <https://doi.org/10.1039/c8cp02512f>.
44. Pearson, R.G. (1963). Hard and soft acids and bases. *J. Am. Chem. Soc.* 85, 3533–3539. <https://doi.org/10.1021/ja00905a001>.
45. Kim, K., Hwang, S., and Lee, H. (2020). Unravelling ionic speciation and hydration structure of  $\text{Fe(III/I)}$  redox couples for thermoelectrochemical cells. *Electrochim. Acta* 335, 135651. <https://doi.org/10.1016/j.electacta.2020.135651>.
46. Li, W., Gao, C., Ma, J., Qiu, J., and Wang, S. (2022). Simultaneous enhancement of thermopower and ionic conductivity for N-type  $\text{Fe(III/I)}$  thermocell. *Mater. Today Energy* 30, 101147. <https://doi.org/10.1016/j.mtener.2022.101147>.
47. Cao, X., Gong, N., Zhao, H., Li, Z., Sun, C., and Men, Z. (2019). Raman spectroscopic study of nonlinear modulation on Fermi resonance of acetonitrile by hydrogen-bonding network. *J. Mol. Liq.* 279, 625–631. <https://doi.org/10.1016/j.molliq.2019.02.016>.
48. Babu, C.S., and Lim, C. (1999). Theory of ionic hydration: insights from molecular dynamics simulations and experiment. *J. Phys. Chem. B* 103, 7958–7968. <https://doi.org/10.1021/jp9921912>.
49. Jung, S.M., Kang, S.Y., Lee, B.J., Lee, J., Kwon, J., Lee, D., and Kim, Y.T. (2023). Fe-N-C electrocatalyst for enhancing  $\text{Fe(II)/Fe(III)}$  redox kinetics in thermo-electrochemical cells. *Adv. Funct. Mater.* 33, 2304067. <https://doi.org/10.1002/adfm.202304067>.
50. Im, H., Kim, T., Song, H., Choi, J., Park, J.S., Ovalle-Robles, R., Yang, H.D., Kihm, K.D., Baughman, R.H., Lee, H.H., et al. (2016). High-efficiency electrochemical thermal energy harvester using carbon nanotube aerogel sheet electrodes. *Nat. Commun.* 7, 10600. <https://doi.org/10.1038/ncomms10600>.
51. Wei, S., Ma, J., Wu, D., Chen, B., Du, C., Liang, L., Huang, Y., Li, Z., Rao, F., Chen, G., et al. (2023). Constructing flexible film electrode with porous layered structure by MXene/SWCNTs/PANI ternary composite for efficient low-grade thermal energy harvest. *Adv. Funct. Mater.* 33, 2209806. <https://doi.org/10.1002/adfm.202209806>.
52. Hess, B., Kutzner, C., Van Der Spoel, D., and Lindahl, E. (2008). GRGMACS 4: Algorithms for highly efficient, load-balanced, and scalable molecular simulation. *J. Chem. Theor. Comput.* 4, 435–447. <https://doi.org/10.1021/ct700301q>.
53. Berendsen, H.J.C., Grigera, J.R., and Straatsma, T.P. (1987). The missing term in effective pair potentials. *J. Phys. Chem.* 91, 6269–6271. <https://doi.org/10.1021/j100308a038>.
54. Aguilar, C.M., De Almeida, W.B., and Rocha, W.R. (2007). The electronic spectrum of  $\text{Fe}^{2+}$  ion in aqueous solution: A sequential Monte Carlo/quantum mechanical study. *Chem. Phys. Lett.* 449, 144–148. <https://doi.org/10.1016/j.cplett.2007.10.063>.
55. Jorgensen, W.L., Maxwell, D.S., and Tirado-Rives, J. (1996). Development and testing of the OPLS all-atom force field on conformational energetics and properties of organic liquids. *J. Am. Chem. Soc.* 118, 11225–11236. <https://doi.org/10.1021/ja9621760>.